

On the crashworthiness of aperiodic chiral mechanical metamaterials: design and modeling method

Weiyun Xu¹, Hanyu Zhang^{1,3}, Zhao Liu² and Ping Zhu^{1,3}

¹ The State Key Laboratory of Mechanical System and Vibration, National Engineering Research Center of Automotive Power and Intelligent Control, School of Mechanical Engineering, Shanghai Jiao Tong University, Shanghai, China.

² School of Design, Shanghai Jiao Tong University, Shanghai, China.

³ Correspondence to Ping Zhu (pzhu@sjtu.edu.cn) and Hanyu Zhang (zhanghanyu@sjtu.edu.cn).

Abstract. Chiral mechanical metamaterial has become topical in energy absorption for the unusual compression-to-twist deformation determined by the asymmetric chirality geometry of their microstructures. However, the insufficient research on the dynamic crash behavior with high nonlinearity and the lack of efficient design and modeling method have blocked the development of chiral mechanical metamaterials considering crashworthiness. In this work, the structure-property relationship of chiral mechanical metamaterials under middle-strain-rate impact was systematically investigated. We proposed an aperiodic framework considering additive manufacturing which enabled both the ordered and disordered chiral mechanical metamaterials utilizing a screw-theory-based assembly rule. The strut components had variable cross-sections and the joints were fillet-enhanced in order to improve the compressive performance. Meanwhile, the corresponding efficient modeling method for finite element analysis (FEA) was introduced. The constitutive relation, damage criteria, and damage evolution of the 316L stainless steel were established considering strain rate effect. Finally, the deformation mechanisms and energy absorbing capabilities of the proposed chiral mechanical metamaterials were demonstrated and discussed based on the mechanical behaviors and the proposed chirality indexes. The numerical results indicated that the proposed design and modeling method provided an effective paradigm for the crashworthiness design of light-weight materials and structures, facilitating the further applications in fields of automobile, civil engineering, aerospace, etc.

1. Introduction

Twist is an essential phenomenon in nature, which plays an important role in structural morphology and stimulation responses. For example, the left-handed/right-handed towel gourd tendrils [1], the twist-tension coupling in DNA structures [2], humidity-driven spider silks [3], and helicoidal structures in beetle elytron and crab [4]. Along with these natural inspirations, last decade has witnessed the development of chiral mechanical metamaterials (CMM) with twist effects [5-11], whose base units are rationally designed to possess the symmetry-broken architectures and unexpected properties [12].

With additional twist degrees of freedom (DOF), CMMs exhibit unique twist-compression or twist-tensile coupling. Various categories of chiral unit cells have been proposed enabling flexible design of deformation patterns [13-15]. However, the mainstream design method of CMM is based on a periodic arrangement of chiral unit cells [16-18], which might restrict the further implementation of CMM in

engineering. As for the other categories of mechanical metamaterials, the aperiodic design has enabled a better damage-tolerant performance by imitating the distribution of metal grains [19] or the graded bio-microstructures in nature [20], whereas the corresponding research on disordered or graded CMM needs to be followed up. Moreover, the periodic boundary conditions of chiral unit cells can inherently cause the unscalable twist effect which diminishes the twist angle as the number of unit cells multiplies [21,22]. Therefore, general and scalable assembly rules need to be proposed to tackle this problem [23], which can be regarded as an aperiodic method.

Considering the extraordinary mechanical performances and light-weight properties of CMM, researches that apply CMM to wave propagation, mode transversion, and energy absorption have been reported [24-26]. For example, the high nonlinear behaviors of flexible CMM tubes were demonstrated by Lipton, J. I. et al. [27], the negative Poisson's ratio of CMM was tailored by Ha, C.S. et al. [28], and a discrete assembly system utilizing CMM was proposed to construct mechanical structures [29]. Focused on the good promise in energy-absorbing, buffering, and shock absorption fields [30-32], the energy absorbing capability of CMM and the underlying mechanisms were further investigated. For instance, based on quasi-static compression tests, large rotation-compression coupled deformations were derived [33]. And tunable normal-strain shear coupling effect was obtained through 2.5D and 3D design [34]. However, the structure-property relationship between the designed geometry and the energy absorption needs for more systematic research. Meanwhile, a drop-weight test was conducted to validate the hyperbolic CMM proposed by Meng, L. et al. [35], but the CMM was 3D-printed by non-metallic material which was impractical. Therefore, despite the promise, the crashworthiness of CMM requires further research regarding the dynamic responses of metal constituent.

This study aims to reveal the deformation mechanism of metal CMM under medium-strain-rate impact, and to explore the inherent connection between the mechanism and the design. Consequently, we proposed a comprehensive design framework that enables the aperiodic design of CMM. Different chiral configurations geometric models along with the finite element models can be generated efficiently and effectively. With research reporting that enhancing the joints by geometric transition like fillet can reduce the stress concentration and thus improve the rigidity and strength of lattice material [36,37], we also introduced a joint-enhanced design under the proposed framework. Based on the insight obtained from the geometrical features, we thereafter demonstrated the chiral indexes which were used to evaluate and characterize the chirality of the designed chiral mechanical metamaterials. Considering the design for additive manufacturing and future application, we chose 316L stainless steel as the constituent material of CMM. By carrying out finite element analysis in multiple cases, the crashworthiness of the proposed CMM was investigated, quantified, and discussed. Not only that, the underlying deformation mechanisms and structure-property relationships were further elucidated.

The article was developed as follows. In section 2, we introduced the proposed aperiodic design framework of chiral mechanical metamaterials. The assembly rules were explained, and the design parameters of joint-enhanced design were illustrated. After that, we proposed the characterization method of chirality using three chiral indexes. In section 3, we demonstrated how the finite element analysis is carried out, including the constitutive model of material, the meshing method, the boundary conditions, etc. In section 4, we showed and discussed the numerical results of the crashworthiness of the proposed CMM. The effect of geometric parameters on impact-resistance was quantified and illustrated. Following that, we drew the conclusions in section 5.

2. Design method of chiral mechanical metamaterials

In this section, we introduced the design framework of chiral mechanical metamaterials (CMM). The concept of instantaneous pseudo rigid body model in mechanics was introduced to obtain the instantaneous degrees of freedom of material microstructures. Then based on screw theory, we proposed that each strut can be characterized as a constraint screw of the given rotate center. We quantified the assembly rule of CMM using mathematical expressions, and obtained scalable twist

effect that enables obvious twist even at large number of unit cells. The design space of geometrical parameters was constructed, the chirality of the metamaterial crystals was characterized, and the assembly rule of chiral unit cells was established. Following that, we proposed the aperiodic design method for the crashworthiness of the metamaterials with enhanced joints.

2.1. Assembly rules for chiral mechanical metamaterials

For chiral mechanical metamaterials (CMM), the description of the additional rotation DOF of chiral geometries is the key point to predict the tension-torsion coupling behavior. In this work, we analyzed the mechanism underlying the twist effects based on screw theory [38], which provides a general but effective way to guide the assembly of chiral unit cells.

The motion or external constraint of a rigid body can be instantaneously decomposed by a translational component along and a rotational component around an instantaneous screw axis (ISA). According to the screw theory, a screw representation can well describe the two components and the corresponding ISA. Considering the compression-to-rotation deformation of chiral unit cell, screw theory enables the use of rigorous algebraic theory to analyze the instant behaviors of CMM assembled by multiple unit cells. Choosing Z-shaped CMM to facilitate demonstration, as illustrated in figure 1, we viewed the CMM as an assembly of Z-shaped base structures, built an instant PRBM [29] for each of the base structures, and characterized the DOF using screw representations.

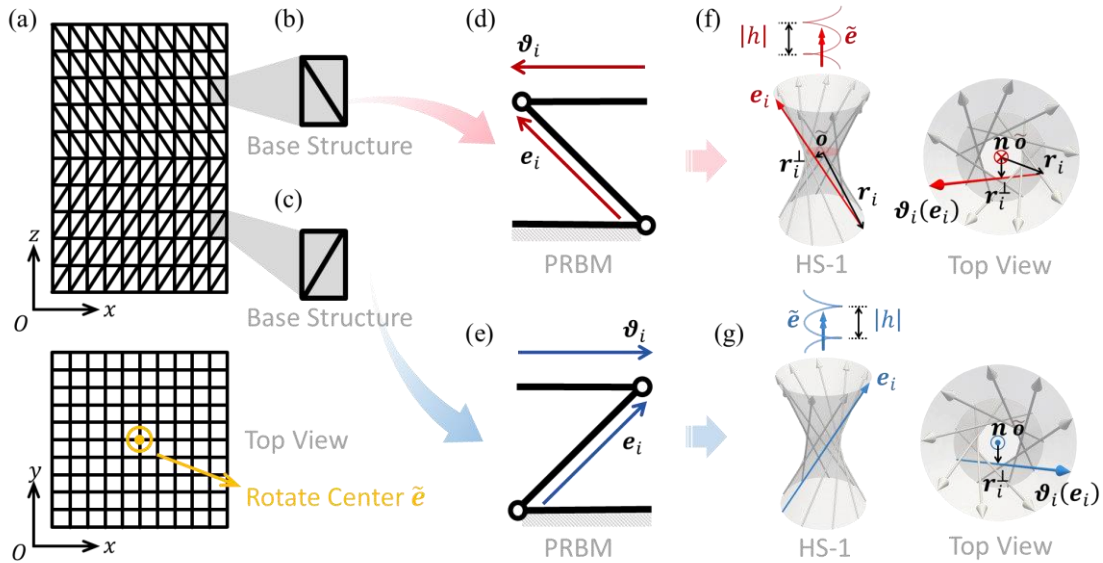


Figure 1. Analysis of chiral mechanical metamaterials based on screw theory. (a) The schematic side view and top view of a 3D Z-shaped CMM. (b) or (c) is the respective base structure of a left-handedness/right-handedness unit cell. (d) and (e) are the instant PRBMs. (f) and (g) are the HS-1 constraint screws characterizing the motion of base structures.

Specifically, a 3D unit cell with twist effects can be further disassembled into 2D base structures, and the DOF of their instant PRBMs can be described by a motion screw $\xi = \omega[\tilde{e}, h\tilde{e}]^T$ with an angular velocity ω , a finite pitch h , and the center line \tilde{e} as its ISA, as shown in figure 1(f) and (g). The constraints within the unit cell can also be described by a set of constraint screws $\{\zeta_i\}$. To achieve the twist DOF ξ , ISA \mathbf{e}_i of each constraint ζ_i should belong to the same branch of straight lines on a hyperbolic surface of one sheet (HS-1) centering around \tilde{e} , i.e., $\zeta_i = [\mathbf{e}_i, \mathbf{r}_i \times \mathbf{e}_i]^T$, where \mathbf{r}_i is a vector connecting the unit-cell center \tilde{o} and a point on ISA. Our investigation [23] has previously elucidated that, by requiring $\tilde{e} \cdot \mathbf{e}_i > 0$, the sign of $\tilde{e} \cdot \mathbf{r}_i \times \mathbf{e}_i$ can be used to differentiate the two branches of straight lines on HS-1, which should be the same for all ζ_i . The pitch of ξ can be obtained as

$$h = \frac{-\tilde{\mathbf{e}} \cdot (\mathbf{r}_i \times \mathbf{e}_i)}{\tilde{\mathbf{e}} \cdot \mathbf{e}_i} = \frac{\mathbf{r}_i^\perp \cdot (\tilde{\mathbf{e}} \times \mathbf{e}_i)}{\tilde{\mathbf{e}} \cdot \mathbf{e}_i}, \quad (1)$$

where $\mathbf{r}_i^\perp = \mathbf{r} \mathbf{e}_{r,i}$ is the vector starting from $\tilde{\mathbf{o}}$ and perpendicularly connecting to the ISA of ζ_i , with a length of r . Based on the analysis, we can obtain that the compatible chirality of a CMM crystal which enables scalable twist effects requires a share screw for all its unit cells, i.e., all unit cells have the same center line $\tilde{\mathbf{e}}$, pitch h , and the branch of HS-1 $\text{sgn}(h)$ [23]. To satisfy the compatibility, it breaks the periodic configuration of the original CMM design. Thus, we present the aperiodic assembly rule to ensure a scalable twist effect of CMM. Given the predefined center line $\tilde{\mathbf{e}}$, the criteria can be expressed as

$$A(\mathbf{r}_i, \mathbf{e}_i) = \text{sgn}(\tilde{\mathbf{e}} \cdot \mathbf{r}_i \times \mathbf{e}_i) = \begin{cases} +1, \text{right handedness} \\ 0, \text{irrotation} \\ -1, \text{left handedness} \end{cases}, \quad (2)$$

where \mathbf{e}_i represents the orientation vector of arbitrary inclined strut within each Z-shaped unit cell and \mathbf{r}_i is the position vector of the strut end point that guarantees $\tilde{\mathbf{e}} \cdot \mathbf{e}_i > 0$. It should be noted that, this rule is applicable to various types of CMM unit cell including O-shaped [7] and #-shaped CMM [14]. Moreover, the handedness of each base structure can be assigned independently, which provides a vast design domain with diverse combinations of chiral geometry and handedness.

2.2. Aperiodic design of chiral mechanical metamaterials

In accordance to equation (2), the assembled CMM can have either an ordered or disordered chiral configuration along center line $\tilde{\mathbf{e}}$, whereas the periodic boundary conditions of the unit cells no longer exist. Inspired by the insight, we further broaden the aperiodic characteristics to the diameter of strut components and the size of chiral unit cells which we will explain in this subsection.

2.2.1. Geometrical features considering additive manufacturing.

Considering the feature of uniaxial crashworthiness test, we present the metamaterial crystals with uniaxial mechanical response which is defined along z-axis in this paper. Therefore, cubic unit cells of $a_x \times a_y \times a_z$ size can be aligned in three principal directions with number N_x , N_y , and N_z respectively, i.e., $N_x \times N_y \times N_z$, as shown in figure 2.

Meanwhile, the design for additive manufacturing (AM) of the CMM crystals should be stressed. Although the experimental result is not presented in this work, emphasizing manufacturability during the design phase is beneficial for future applications and validation. For this reason, we chose the fundamental Z-shaped unit cell [9,35,39] to facilitate demonstration. In existing CMM designs, the category of Z-shaped chiral unit cell shows a good compression-to-twist performance [10] and embodies in various types of chiral metamaterials [13]. And it is composed of strut-based structures with Z-shaped motif which is easier to fabricate by AM. Before stepping further, we adapted the geometry of CMM to suit the manufacturing constraints of selective laser melting (SLM) technique. By canceling all the transverse struts (the crossbars of the Z-shaped unit cell) and adding the vertical struts instead, the self-support design for metal SLM can be obtained as shown in figure 2(d). Under the geometric features, we pre-tested the manufacturable geometrical parameters by printing a batch of strut samples that varied in diameter, cross section shape, and inclined angle, as shown from top to bottom respectively in figure 2(f). By detecting the forming quality and avoiding obvious printing defect, this procedure enables the reliable fabrication of CMM samples for experimental validation in the future. It also served as the guideline to construct the CMM design domain of geometrical parameters as shown in figure 2(h), which benefited the general design framework of CMM.

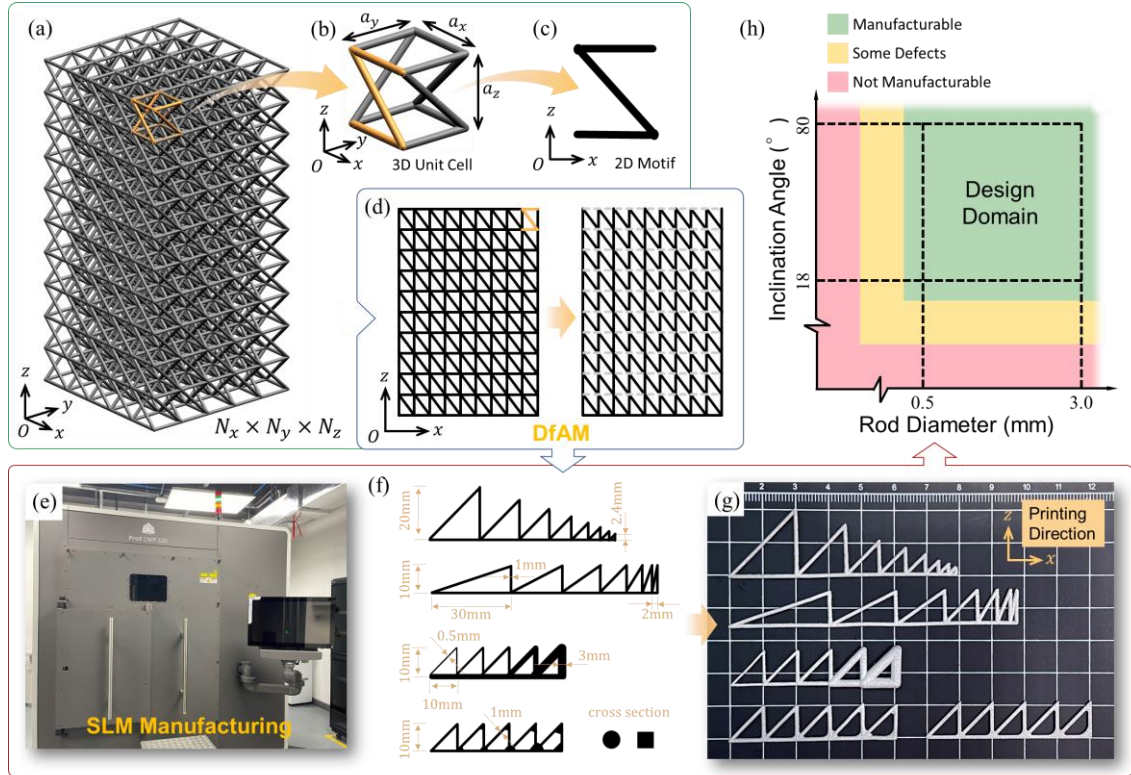


Figure 2. The basic geometry of chiral mechanical metamaterials and the basic design domain. (a) Original CMM crystal arranged periodically by (b) the Z-shaped unit cell which can be further disassembled into (c) 2D Z-shaped motifs. (d) Schematic side view of the original and the self-support CMM. (e) The metal SLM machine ProX-DMP320 used in this work. (f) The dimension of strut structures and (g) the corresponding fabricated samples to pre-test the manufacturable geometrical parameters. (h) The basic design domain constructed by proper intervals of the rod diameter and the inclination angle.

The process parameters including laser power, scanning velocity, temperature, etc., were guided by the equipment manufacturer. Via the pre-test, we constructed the basic design domain of the diagonal strut with respect to the rod diameter and inclination angle, which was constrained as $[0.5\text{mm}, 3.0\text{mm}]$ and $[18^\circ, 80^\circ]$ respectively.

2.2.2. Aperiodic framework of CMM. Under the aforementioned design constraints, we propose the aperiodic design framework referring to figure 3. Specifically, this method is divided into three steps: seeding, connecting, and enhancing. Firstly, in the seeding step, we can define $(N_x + 1) \times (N_y + 1) \times (N_z + 1)$ of spherical joints – the geometry that connect the ends of multiple struts – within the space occupied by the overall size of CMM crystals. Denoted as $J_{i,j,k}$, the i -th, j -th, and k -th joint along x-axis, y-axis, and z-axis respectively can have independent value of diameter. If the distance between adjacent joints varies for different locations, it can intuitively form an irregular distribution such as graded or disordered configuration. Conversely with the same distance, a regular distribution with uniform unit-cell length is generated.

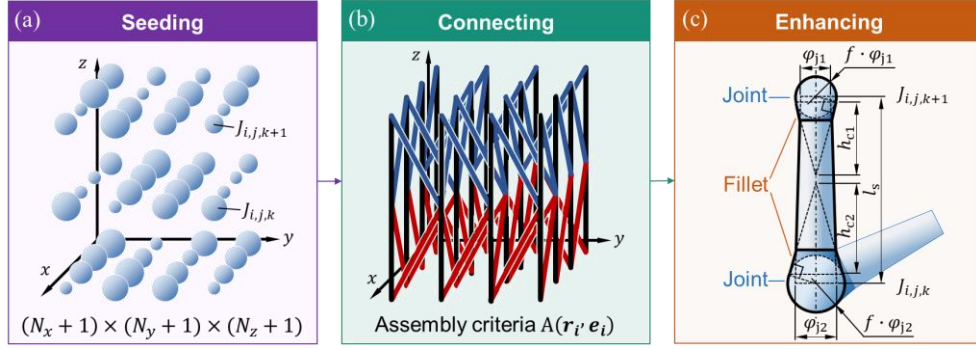


Figure 3. Aperiodic design framework of chiral mechanical metamaterials where the schematic illustrations of (a) seeding, (b) connecting, and (c) enhancing steps are shown.

Next in connecting step, we can define the connect relationships between joints to design the chiral geometry of CMM. As illustrated in figure 3(b), the rods connecting joints contain vertical struts and diagonal struts. The handedness of diagonal component is determined according to the proposed assembly criteria $A(\mathbf{r}_i, \mathbf{e}_i)$, contributing to the overall chirality. With uniaxial twist response, the CMM crystal can be viewed as a combination of multiple z -directional layers, and the chirality of each layer can be tailored independently. Thus, we defined the handedness average of each layer referring to equation (2) as:

$$c_{k,Z} = \frac{1}{B_{k,Z}} \sum A(\mathbf{r}_i, \mathbf{e}_i), c_{k,Z} \in [-1, +1], \quad (3)$$

where $B_{k,Z}$ is the number of base structures in the k -th layer. In this way, the chirality of the CMM can be defined as:

$$\mathbf{C}_Z = [c_{k,Z}]_{1 \times N_Z} \quad (4)$$

which we named Assembly Matrix to guide the design.

2.2.3. Joint-enhanced design with variable cross-section strut. With the geometric parameters of the joints and the connecting information defined, we can generate the geometry of the strut components in the enhancing step as shown in figure 3(c). If the joints have unified diameter, i.e., $\varphi_{j1} = \varphi_{j2}$, the strut is a cylinder determined by the diameter and the relative distance of joints l_s ; if the joints in the two ends of a strut component differs in diameter, i.e., $\varphi_{j1} \neq \varphi_{j2}$, the strut is then a circular truncated cone instead with height l_s .

Finally, the enhanced joints can be well adapted in the proposed design method. Specifically, we enlarged the joint by a multiply factor f denoted as enlarge factor, and generate the transition geometry between the joint and the strut by a cone with a bottom diameter of $f\varphi_j$ and a height of h that is defined by a coefficient μ as:

$$h = \mu f l_0 \quad (5)$$

where l_0 is the reference length of strut component which is set as the length of the shortest one. we named μ the height coefficient, which is fixed as 0.125 in this work. The cone-shape fillet provides a practical enhancement for the joint in this aperiodic design.

2.3. Characterization of chirality

To further demonstrate the presented design method, we specifically determined the geometrical parameters to generate CMM that are fundamental under the manufacturing constraints. Therefore, we set the joints as $(N_x + 1) \times (N_y + 1) \times (N_z + 1) = 10 \times 10 \times 11$, with unified unit-cell size as $a_x \times a_y \times a_z = 6\text{mm} \times 6\text{mm} \times 10\text{mm}$. It is noted that the number of joints is one more than that of unit cells in each principal direction. Besides, we defined unified diameter $\varphi_{j1} = \varphi_{j2} = 1\text{mm}$ ($d = 1\text{mm}$) and the enlarge factor $f = 2.0$. As shown in figure 4, three representative configurations of CMM were designed by determining the assembly matrix \mathbf{C}_Z with their CAD models generated by

commercial software NX UG 12.0. Referred as mirrored chirality, mixed chirality, and achiral configuration respectively, their bottom and top were fixed with panels of size 70mm × 70mm × 2mm to guarantee a unified boundary condition.

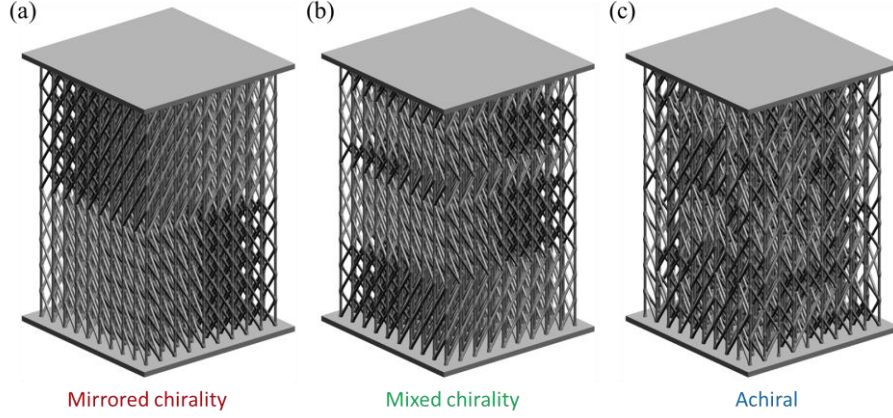


Figure 4. Three representative configurations of the proposed CMM: (a) Mirrored chirality. (b) Mixed chirality. (c) Achiral configuration.

Firstly, the assembly matrix of mirrored chirality is $[+1, +1, +1, +1, +1, -1, -1, -1, -1, -1]$. With the first 5 layers right-handed and the last 5 layers left-handed, the top and bottom panels are expected irrotational whereas the CMM rotates in response to the compressive displacement. Secondly, the mixed chirality is a more general configuration with more reverse changes of handedness between layers. The particular \mathbf{C}_Z in figure 4(b) is $[+1, +1, +1, -1, -1, -1, +1, -1, -1, +1]$. It is also irrotational at the upper or lower boundary due to the offset of chirality among layers as $\sum c_{k,Z} = 0$. Based on this insight, the achiral configuration can be designed by randomly assigning handedness of every strut and requiring $\sum c_{k,Z} = 0$. One from this category is shown in figure 4(c) with $c_{k,Z} = [-23, 14, 2.2, 6.7, 2.2, -6.7, 2.2, 5.6, -4.4, 1.1] \times 10^{-2}$. We expect the achiral CMM exhibits no overall twist DOF, the result of which will be presented and discussed in section 4.

With various configurations that the design method can generate, do they have distinguished crashworthiness performance with respect to energy absorption or deformation patterns? As mentioned in this introduction, few research has characterized the chirality of chiral materials or structures in a rigorous way. However, a closed form of chiral expression helps the generality of CMM design and facilitates a fair comparison among various categories of CMM. Herein, we evaluated the chiral geometry of CMM by mathematically describing the overall chirality (OC), deviation of chirality (DC), and the consistency of chirality between layers (CC).

Specifically, inspired by the orientation tensors in mean-field homogenization (MFH) of composite materials [40], we introduced the chiral index to measure the overall chirality of metamaterial crystals generated by the proposed design method. Suppose $\mathbf{p}_i = \hat{\mathbf{r}}_i \times \mathbf{e}_i$ is the chiral vector of arbitrary inclined strut in unit cells where $\hat{\mathbf{r}}_i$ is the projective vector of \mathbf{r}_i in the plane perpendicular to the rotation center $\tilde{\mathbf{e}}$. With various chiral unit cells distributed in the CMM crystal, \mathbf{p}_i forms an orientation-dependent field inside the metamaterial, denoted as $\mu(\mathbf{p}_i)$. In this way, each chiral microstructure has an oriented description in Cartesian coordinate. Its orientation average is the integral over all orientations, weighted by the orientation distribution function $\Psi(\mathbf{p}_i)$:

$$\langle \mu(\mathbf{p}_i) \rangle_\Psi = \oint \mu(\mathbf{p}_i) \Psi(\mathbf{p}_i) d\mathbf{p}_i. \quad (6)$$

Thus, the index is defined as the following orientation average:

$$\alpha_Z \equiv \langle \mathbf{p}_i \otimes \mathbf{p}_i \rangle_\Psi. \quad (7)$$

It can be derived that α_Z is a symmetric second-rank tensor and measures the overall chirality of CMM, namely OC. With fixed geometric parameters, OC is influenced by the arrangement of chiral base structures.

Meanwhile, analogy to variance in statistics, DC describes the deviation of chirality of each layer with the overall chirality, expressed as

$$\beta_Z = \frac{1}{N_Z} \sum (c_{k,Z} - c)^2, c = \frac{1}{N_Z} \sum c_{k,Z}, \beta_Z \in [0, +1]. \quad (8)$$

Referring to equation (8), the bigger DC, the higher deviation. And CC describes the consistency of chirality in adjacent layers as:

$$\gamma_Z = \prod e^{-\frac{|c_{k,Z} - c_{k+1,Z}|}{N_Z}}, \gamma_Z \in [0, +1]. \quad (9)$$

Equation (9) indicates that the CMM with good consistency has a γ_Z close to 1. Following that, the characterizations of the three configurations are listed in table 1 along with the relative density (RD) derived by:

$$\frac{\rho^*}{\rho_s} = \frac{V_m}{V_s} \times 100\%. \quad (10)$$

Table 1. Characterization of the chirality of the proposed CMM.

Configuration	OC, α_Z	DC, β_Z	CC, γ_Z	RD, ρ^*/ρ_s
Mirrored	$\begin{bmatrix} 0.4105 & 0.0000 & 0.0000 \\ 0.0000 & 0.4105 & 0.0000 \\ 0.0000 & 0.0000 & 0.1789 \end{bmatrix}$	1.0000	0.8187	8.89%
Mixed	$\begin{bmatrix} 0.4105 & 0.0000 & 0.0000 \\ 0.0000 & 0.4105 & 0.0000 \\ 0.0000 & 0.0000 & 0.1789 \end{bmatrix}$	1.0000	0.4493	8.89%
Achiral	$\begin{bmatrix} 0.4127 & 0.0028 & 0.0065 \\ 0.0028 & 0.4096 & 0.0035 \\ 0.0065 & 0.0035 & 0.1777 \end{bmatrix}$	0.0091	0.9089	8.71%

It can tell from the table that the three CMMs have close or even the same OC. All with $\sum c_{k,Z} = 0$, the left/right handedness in each layer of mirrored or mixed type has a serious deviation indicated by DC, while the achiral CMM is literally achiral everywhere. Moreover, CC of the mirrored CMM is bigger than that of the mixed one, implying that there exist more changes of layer handedness in the latter configuration. In section 4, we will discuss the impact of these proposed chiral indexes on energy absorption and crush deformation.

3. Finite element analysis of chiral mechanical metamaterials

Another aspect of the proposed CMM generation framework is the modeling method for finite element analysis (FEA). In this section, we introduced the details of FEA utilizing ABAQUS, including the constitutive model, the boundary conditions, the interaction settings, and the meshing method.

3.1. Johnson-Cook constitutive model of 316L

In this paper, the 3D-printed stainless steel AISI 316L was applied to construct the chiral mechanical metamaterials. The high ductility of 316L is ideal for energy absorption due to the more plastic dissipation compared with brittle materials. The chemical composition of SLM 316L is shown in table 2 referring to literature [41]. Meanwhile, the density is set as 7.98 g/cm³.

Table 2. The chemical composition of SLM 316L stainless steel (wt. %) [41].

Material	%C	%Si	%Mn	%Ni	%Cr	%Mo	%Cu	%S	%N
316L SS	0.03	0.059	1.04	10.35	16.5	2.034	0.32	0.004	0.098

Considering the large deformation and high strain rate of the impact process, we used Johnson-Cook (J-C) constitutive model to characterize the mechanical behavior of 316L.

3.1.1. *The J-C plasticity model.* The J-C plasticity model describes the plastic behavior of materials where the yield stress is determined by the strain, the strain rate, and the temperature. The general formula [42] is

$$\sigma = \left[A + B(\bar{\epsilon}^{pl})^n \right] \left[1 + C \ln \left(\frac{\dot{\epsilon}^{pl}}{\dot{\epsilon}_0} \right) \right] \left[1 - \left(\frac{T - T_0}{T_M - T_0} \right)^m \right] \quad (11)$$

where σ is the equivalent plastic stress, $\bar{\epsilon}^{pl}$ is the equivalent plastic strain, and $\dot{\epsilon}^{pl}$ and $\dot{\epsilon}_0$ are the strain rate and the reference strain rate respectively. A , B , C , n , and m are the constants of J-C model, which respectively represents the initial yield stress, hardening modulus, strain rate constant, hardening exponent, and thermal softening exponent. Without temperature effect taken into account, equation (11) can be simplified as follows:

$$\sigma = \left[A + B(\bar{\epsilon}^{pl})^n \right] \left[1 + C \ln \left(\frac{\dot{\epsilon}^{pl}}{\dot{\epsilon}_0} \right) \right]. \quad (12)$$

3.1.2. *The J-C failure model.* The J-C failure model without temperature effect is expressed as [41]

$$\epsilon_f = [D_1 + D_2 \exp(D_3 \eta)] [1 + D_4 \ln(\dot{\epsilon}_p^*)] \quad (13)$$

where $\dot{\epsilon}_p^* = \dot{\epsilon}^{pl} / \dot{\epsilon}_0$, η is the triaxiality, and D_1 , D_2 , D_3 , and D_4 are the failure constants. The constants in the plasticity model and failure model can be measured and calculated through a series of tests with different test samples at different loads and strain rates, which has been systematically studied in literatures. Herein we used the constants reported in [41] and [42], as listed in table 3.

Table 3. Constants of the 316L J-C constitutive model ($\dot{\epsilon}_0 = 0.001s^{-1}$).

A (MPa)	B (MPa)	n	C	D_1	D_2	D_3	D_4
554.05	3919.72	1.17	0.0118	0.4	120	-15	-0.025

The energy damage evolution was defined to characterize the failure after the initiation of damage, which can be described as:

$$D = \int \frac{dG_f}{G_{fc}(\theta, \bar{\epsilon}^{pl})} = 1$$

$$G_f = \int_{\bar{\epsilon}_0^{pl}}^{\bar{\epsilon}_f^{pl}} L \sigma d\bar{\epsilon}^{pl} \quad (14)$$

3.2. Meshing of CMM crystals

To establish a FEA model of high fidelity, traditional finite element modeling method may discretize the CAD model directly by solid elements, which is unacceptable in computational efficiency. In fact, the proposed CMM crystals (figure 4) meshed by tetrahedron elements exceeded the computing power of our computers (over 20 million elements) and has a bad meshing quality of the joints. Therefore, we herein used a simplified meshing method to build CAE models (FEA models) from the CAD ones as illustrated in figure 5.

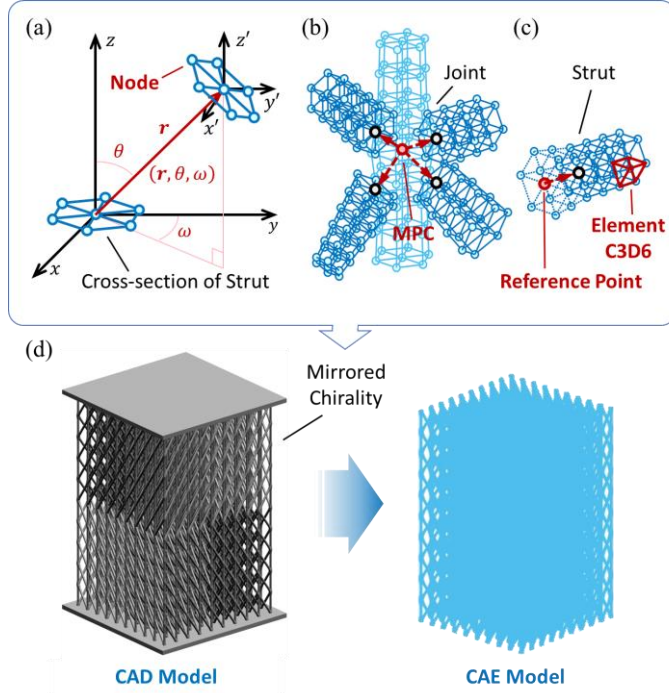


Figure 5. FEA modeling method of the proposed CMM crystals. (a) Coordinate transformation of pre-defined cross-section nodes. (b) The constraints of a joint using MPC. (c) The mesh of a variable cross-section strut component using C3D6 elements. The reference point couples the nodes at the end of the strut. (d) A CAE model meshed from a CAD model. The mirrored chirality is chosen for illustration.

Specifically, we first defined the concept that, each strut component along with the enhanced joints at its two ends is meshed respectively. After that, the components are assembled by constraints in accordance to the pre-defined connection relationships. All struts were meshed using the C3D6 wedge elements in ABAQUS considering the accuracy and efficiency. Secondly, we define the number of elements that is used to mesh the cross-sections. With strut diameter $d = 1\text{mm}$ and enlarge factor $f = 2.0$ in this work, the approximate global size of element is set as 0.5mm after convergence analysis. In this way, the circular section is approximating to a polygon, such as a hexagon or octagon. Thirdly, the nodes within a section are defined in a local coordinate and then mapped into the global coordinate based on the position and orientation of the strut, which is described by (r, θ, ω) as shown in figure 5(a). The corresponding coordinate transformation can be expressed as follows:

$$[x' \ y' \ z' \ 1]^T = \mathbf{T} \cdot [x \ y \ z \ 1]^T \quad (15)$$

where (x, y, z) and (x', y', z') are the local and global coordinates of arbitrary node respectively. And the transformation matrix is obtained as:

$$\begin{aligned} \mathbf{T} &= \mathbf{T}_r(\mathbf{r}) \cdot \mathbf{R}_z(-\omega) \cdot \mathbf{R}_x(-\theta) \\ \mathbf{T}_r(\mathbf{r}) &= \begin{bmatrix} 1 & 0 & 0 & dx \\ 0 & 1 & 0 & dy \\ 0 & 0 & 1 & dz \\ 0 & 0 & 0 & 1 \end{bmatrix} \\ \mathbf{R}_x(\varphi) &= \begin{bmatrix} 1 & 0 & 0 & 0 \\ 0 & \cos \varphi & -\sin \varphi & 0 \\ 0 & \sin \varphi & \cos \varphi & 0 \\ 0 & 0 & 0 & 1 \end{bmatrix} \\ \mathbf{R}_z(\varphi) &= \begin{bmatrix} \cos \varphi & -\sin \varphi & 0 & 0 \\ \sin \varphi & \cos \varphi & 0 & 0 \\ 0 & 0 & 1 & 0 \\ 0 & 0 & 0 & 1 \end{bmatrix} \end{aligned} \quad (16)$$

Then, the wedge elements can be defined by matching the nodes between adjacent cross-section. Finally, with each strut component discretized, the multiple point constraint (MPC) was applied to assemble the FEA model of CMM, as demonstrated in figure 5(b). Following the meshing method, the

element number was reduced to 3.5-4 Million, and it was efficient via replacing the heavy manual operation in modeling by automatic parametrical process.

3.3. Model settings and boundary conditions of FEA

With the material properties set and meshing method applied, we can continue to conduct the FEA of the uniaxial crash simulation. In this work, the dynamic responses of the proposed CMM were analyzed utilizing ABAQUS Explicit. In the step settings, the target time increment was set as 1×10^{-6} . As for the boundary conditions, the metamaterial crystal was fixed in the bottom and set free in the top, with a rigid wall conducting axial collision with it. Meanwhile, the contact interaction of the CMM crystals was defined as a hard contact behavior in normal direction and a tangential behavior with friction coefficient of 0.5.

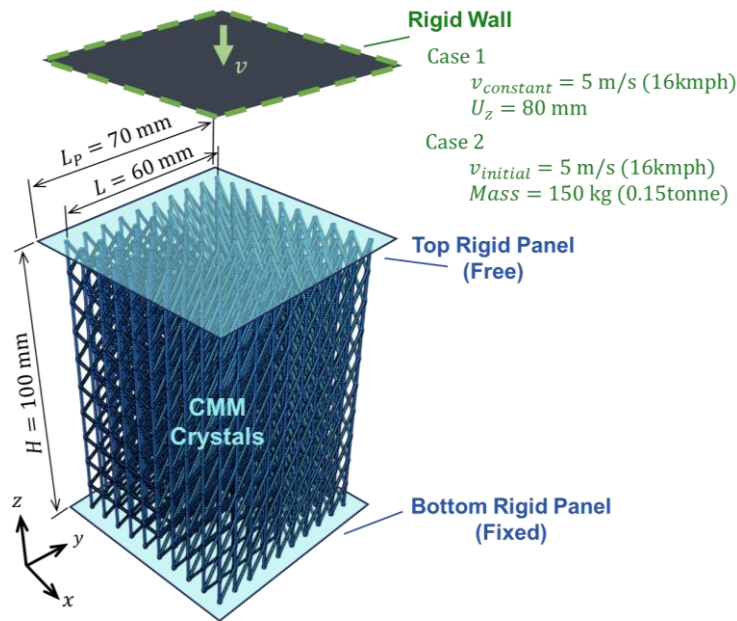


Figure 6. The boundary conditions of CMM crystals in FEA.

We set two operating conditions to carry out a comprehensive study on the crashworthiness of CMM. As illustrated in figure 6, in case 1, the top panel is colliding with a rigid wall that moves 80mm along z-axis with a constant velocity of 5m/s, whereas in case 2, the rigid wall is 150kg weight with an initial velocity of 5m/s. It is noted that the rigid wall is large enough to cover the collision area of CMM. The first case investigates the compressive response of CMM and through the second one we can calculate the displacement of different CMMs with the same initial kinetic energy. The results were post-processed as force-displacement curves and force-time curves by extracting the forces and displacements of the top panels. And the energy absorption (EA) can be calculated as:

$$EA = \int_0^{s_{ple}} F ds \quad [J], \quad (17)$$

where s is the displacement at the end of the yielding platform of CMM. The specific energy absorption (SEA) can be thus derived as:

$$SEA = \frac{EA}{\rho^*} = \frac{\int_0^{s_{ple}} F ds}{\rho_s \cdot \rho^* / \rho_s} \quad [J \cdot m^3/kg], \quad (18)$$

where $\rho_s = 7.98 \text{ g/cm}^3$.

4. Results and discussion

In this section we first show the numerical results of the uniaxial collision. The mechanical behaviors of the three proposed CMM configurations were demonstrated through a comprehensive comparative analysis of initial peak compressive force, mean crush load, collapse displacement, and SEA. Following that, we further investigated the deformation modes of the CMM, and quantified the crashworthiness performances using the proposed chiral indexes. Finally, the effectiveness of the aperiodic design with enhanced joints was illustrated.

4.1. Crashworthiness of CMM

As illustrated in figure 7, under case 1 introduced in subsection 3.3, the stress distribution and the corresponding force-displacement ($F-s$) curve of mirrored, mixed, and achiral configurations respectively exhibit the dynamic response of the proposed CMM. Generally, the CMMs have an initial peak force of 60–70 kN at 0.5%–1.0% axial strain, and undergo a long and steady yielding platform until densification at around 75% axial strain. The axial strain is calculated as $\varepsilon_{zz} = 100 \cdot s/H = s$ [%]. And the mean crush load during yielding platform is 20–30 kN. As presented in subsection 2.2, the CMM designed under the proposed framework can be mainly disassembled into vertical struts and diagonal struts. The former serves as the structural frame with stretching-dominated behavior and the latter forms the chiral geometry with bending-dominated behavior [43]. Therefore, the vertical struts attribute to the large initial peak load, and then drop in force with the plastic buckling. It can be implied that the vertical strut components should incline a certain angle to tailor the $F-s$ curve with lower peak force.

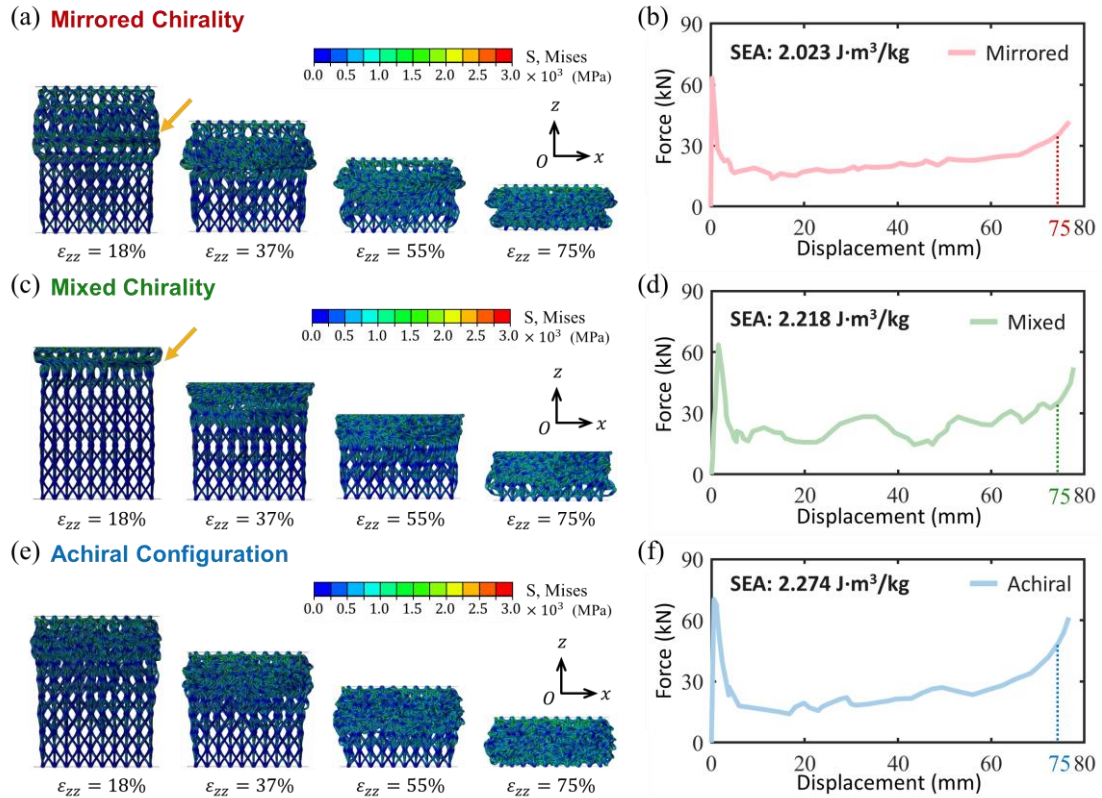


Figure 7. The mechanical responses of the proposed CMM under case 1. (a) The Mises stress distribution of mirrored CMM at $\varepsilon_{zz} = 18\%$, 37% , 55% , and 75% . (b) The force-displacement curve of mirrored CMM. Similarly, the stress distribution and force-displacement curve of mixed and achiral CMM are displayed in (c) and (d), and (e) and (f) respectively. The arrows in (a) and (c) mark the initiate of plastic buckling.

We now take a close look at the absorbed energy in this crush procedure. The respective SEA is shown in figure 7 (b, d, and f) referring to equation (18) with $s_{ple} = 75\text{mm}$. It can tell that under the particular geometric parameters in this paper, the three configurations absorb energy at the same level with the 11% maximum difference. To explain this, the similar OC (table 1) indicates their similar strut orientations and thus similar plastic dissipation in energy during compressive deformation. Theoretically, with diameter of the strut components fixed, CMM with the same OC may have the equivalent energy absorption due to the overall similar bending deformation of all the diagonal strut. And to improve the energy absorption performance, you should change the aspect ratio of each unit cell. The equivalent SEA of mirrored, mixed, and achiral CMM can also be indicated from the force-time ($F - t$) curves in case 2 as shown in figure 8, where they all stop the rigid wall at the same tendency.

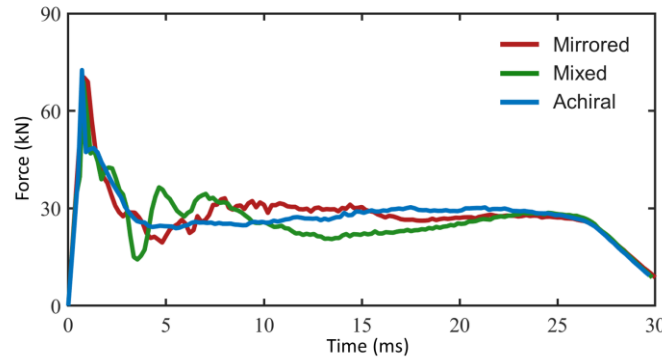


Figure 8. The force-time curves of the mirrored, mixed, and achiral CMM in case 2.

Nevertheless, the crashworthiness of the three configurations differs in the deformation mode, as illustrated in figure 7 (a, c, and e) and figure 9. Compared with the uniform deformation in static conditions, localized buckling of struts was observed as the axial displacement got bigger. It also showed a layered distribution of yield and the struts buckled first where the chirality of adjacent layers inversed. With more layer handedness changes (the bigger CC), the mixed CMM exhibited more twist deformation area than the mirrored one. Moreover, no special deformation mode was observed in the achiral CMM (DC tends to zero). This phenomenon consisted with the mechanism embodied in the indexes DC and CC.

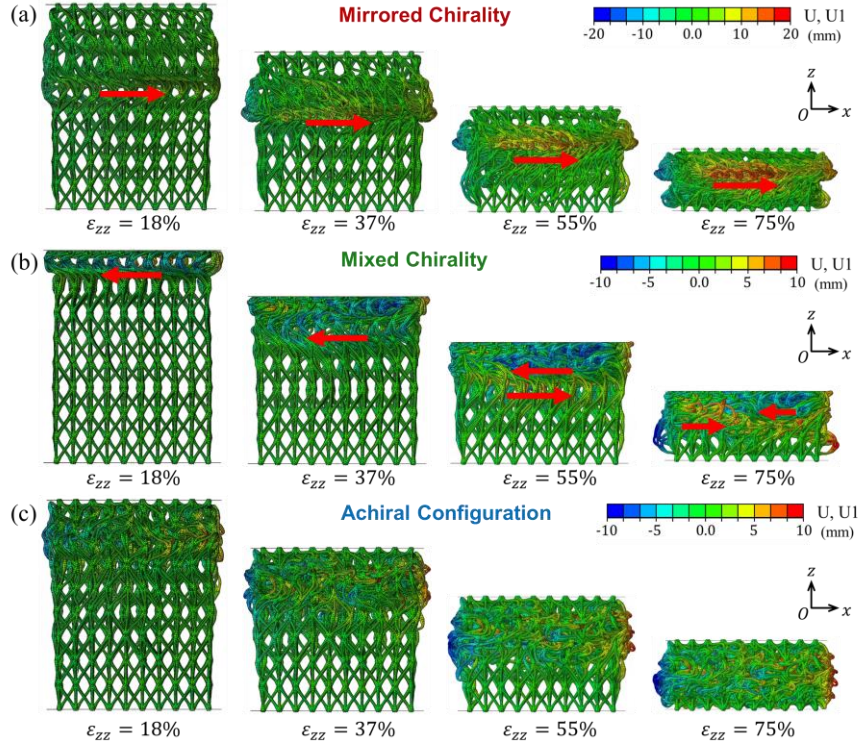


Figure 9. The deformation mechanism of (a) mirrored, (b) mixed, and (c) achiral CMM in case 1. The fields of displacement component U_1 (x-axis) at $\varepsilon_{zz} = 18\%$, 37% , 55% , and 75% are illustrated.

The deformation mechanism can be analyzed via the displacement fields in figure 9. The more inconsistent, the more localized rotation. As a result, CMM with mixed chirality has the most twist deformation of the three.

4.2. Effect of enhanced joints

The effectiveness of the proposed joint-enhanced method is also demonstrated. As mentioned in subsection 2.2, the diameter of enhanced joint is defined as $f\varphi_j$, thus the joints keep original as f becomes 1. Herein, we generated the mirrored CMM with different enlarge factor: $f = 2.0$, $f = 1.5$, and $f = 1.0$. In this approach, we can investigate the influence of the reinforcement of joint on the compressive behavior. Set as in case 2, the corresponding $F - s$ and $F - t$ curves are shown in figure 10.

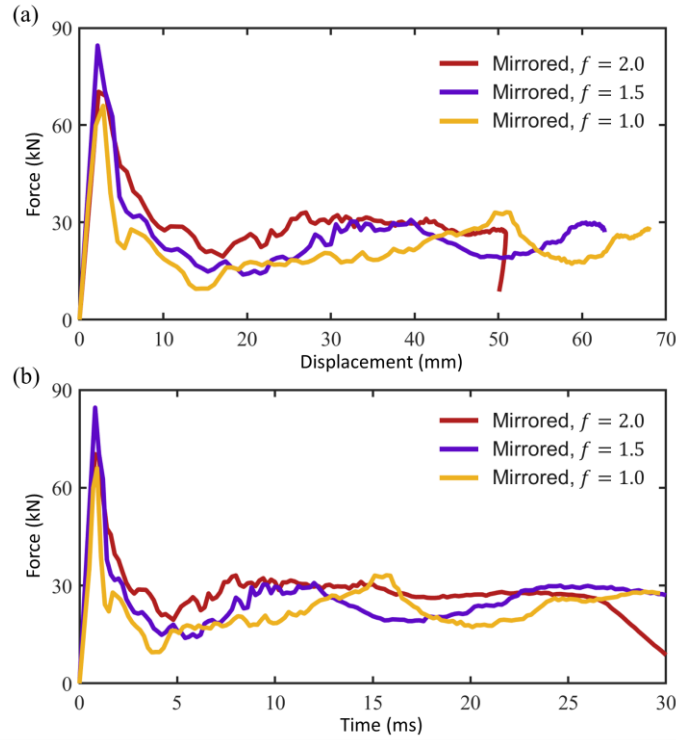


Figure 10. (a) $F - s$ and (b) $F - t$ curves of mirrored CMM with different enlarge factors f in case 2.

From the results, we can observe a smaller collapse displacement along with a smaller response time of CMM with enhanced joints. Calculated as $Mass \cdot v_{initial}^2/2$, the total 1875J kinetic energy was absorbed by the mirrored CMM with $f = 2.0$ at a displacement of 50mm. Meanwhile, CMM with bigger f has higher yield platform. Compared with the CMM that has no enhanced joint, larger joint geometry contributes to less stress concentration around the joint area, thus exhibits a better response to crush.

Furthermore, we have tested the EA with respect to the strut diameter in case 1. As demonstrated in figure 11(a), we can find that thicker strut diameter causes much higher compressive force and earlier densification stage. By studying the correlation between the absorbed energy and the diameter, it is indicated that the EA of the proposed CMM is roughly proportional to the cubic power of the strut diameter.

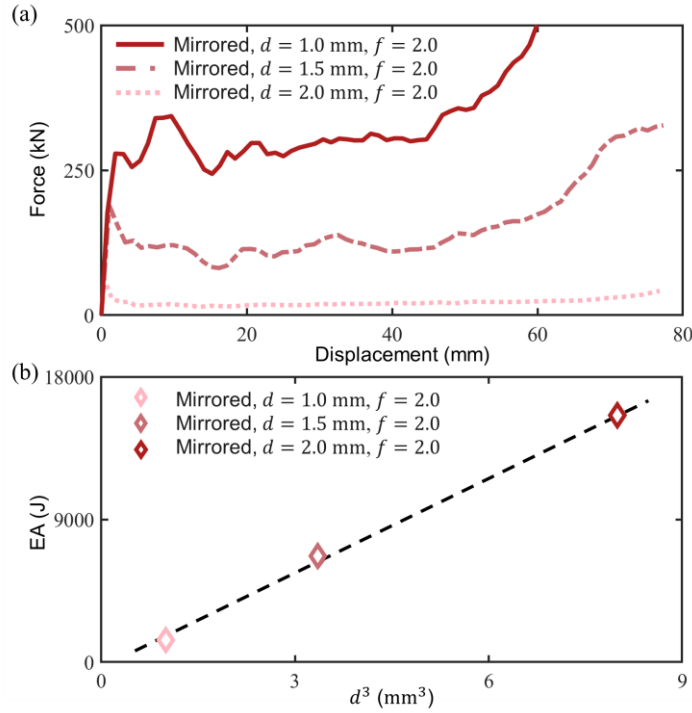


Figure 11. The mechanical responses of mirrored CMM with different strut diameters d in case 1. (a) $F - s$ curves. (b) The absorbed energy with respect to the cubic power of diameter.

5. Conclusions

In this work, we proposed an aperiodic design framework of chiral mechanical metamaterials with enhanced joints which enables a flexible design domain to tailor the lattice architectures. Ordered/disordered and unified/graded metamaterials with different degrees of chirality can be generated. We also demonstrated a FEA modeling method to balance the accuracy and efficiency of high-fidelity simulations.

Next, we characterized the chirality of chiral mechanical metamaterials under the design framework based on screw-theory-based analysis. We quantified the geometrical features via three indexes which respectively describe the total chirality, the deviation, and the consistency between layers. The results indicate that these indexes imply physical meanings and have guiding significance for comparing and explaining the performance of CMM with different configurations.

Finally, we have investigated the crashworthiness of chiral mechanical metamaterials under low-speed impact. Results showed that the absorbed energy depends on the diameter of the strut components, the overall chirality, and the enhancement of joints. We concluded that the SEA of CMM can be elucidated in the overall chirality. And it also illustrated a third-order nonlinear correlation between the diameter and the energy absorption. The deformation mechanism presented an insight on the structure-property relationship of metamaterial.

The results indicated that the proposed design and modeling method provided an effective paradigm for the crashworthiness design of light-weight materials and structures, facilitating the further applications in fields of automobile, civil engineering, aerospace, etc. It should be noted that, we demonstrated the proposed method through the particular parameter settings which were fundamental and uniform. The generality of the design framework can be further explored and discussed by applying it to more categories of CMM, using geometrical parameters that vary from place to place, or assembling the base chiral structures into crystals with more complex shape. Future work may include developing a computational way to obtain the properties of CMM more efficiently

(e.g., AI based methods), optimizing the SEA of CMM via functional graded optimization (FGO), and applying the proposed CMM to energy absorber as fill-in materials (e.g., crush box).

CRedit authorship contribution statement

Weiyun Xu: Conceptualization, Methodology, Software, Writing- Original draft preparation. **Hanyu Zhang**: Visualization. Writing- Reviewing and Editing. **Zhao Liu**: Data curation. **Ping Zhu**: Investigation. Supervision.

Competing interests

The authors declare no competing interests.

Acknowledgments

This work was sponsored by Natural Science Foundation of Shanghai (Grant No. 21ZR1431500 and No. 23ZR1431600).

Data availability

All data needed to evaluate the conclusions in the paper are present in the paper.

References

- [1] Wang J S et al. Hierarchical chirality transfer in the growth of towel gourd tendrils. *Sci. Rep.* **3** (2013). <https://doi.org/10.1038/srep03102>
- [2] Gross P et al. Quantifying how DNA stretches, melts and changes twist under tension. *Nat. Phys.* **7**, 731-736 (2011). <https://doi.org/10.1038/nphys2002>
- [3] Liu D et al. Spider dragline silk as torsional actuator driven by humidity. *Sci. Adv.* **5**, eaau9183 (2019). <https://doi.org/10.1126/sciadv.aau9183>
- [4] Cohen N and Eisenbach C D. Humidity-driven supercontraction and twist in spider silk. *Phys. Rev. Lett.* **128**, 098101 (2022). <https://doi.org/10.1103/PhysRevLett.128.098101>
- [5] Cheng L, Thomas A, Glancey J L and Karlsson A M. Mechanical behavior of bio-inspired laminated composites. *Compos. Pt. A-Appl. Sci. Manuf.* **42**, 211-220 (2011). <https://doi.org/10.1016/j.compositesa.2010.11.009>
- [6] Ha C S, Plesha M E and Lakes R S. Chiral three-dimensional isotropic lattices with negative Poisson's ratio. *Phys. Status Solidi B-Basic Solid State Phys.* **253**, 1243-1251 (2016). <https://doi.org/10.1002/pssb.201600055>
- [7] Frenzel T, Kadic M and Wegener M. Three-dimensional mechanical metamaterials with a twist. *Science* **358**, 1072-1074 (2017). <https://doi.org/10.1126/science.aao4640>
- [8] Yu X, Zhou J, Liang H, Jiang Z and Wu L. Mechanical metamaterials associated with stiffness, rigidity and compressibility: A brief review. *Prog. Mater. Sci.* **94**, 114-173 (2018). <https://doi.org/10.1016/j.pmatsci.2017.12.003>
- [9] Ziemke P, Frenzel T, Wegener M and Gumbsch P. Tailoring the characteristic length scale of 3D chiral mechanical metamaterials. *Extreme Mech. Lett.* **32**, 100553 (2019). <https://doi.org/10.1016/j.eml.2019.100553>
- [10] Xu W, Liu Z, Wang L and Zhu P. 3D chiral metamaterial modular design with highly-tunable tension-twisting properties. *Mater. Today Commun.* **30** (2022). <https://doi.org/10.1016/j.mtcomm.2021.103006>
- [11] Chen X, He T, Hu Y and Feng M. A 3D dislocated re-entrant structure with compression-twist coupling effect. *Smart Mater. Struct.* **32**, 055009 (2023). <https://doi.org/10.1088/1361-665x/acc621>
- [12] Jiao P. Mechanical energy metamaterials in interstellar travel. *Prog. Mater. Sci.* **137**, 101132 (2023). <https://doi.org/10.1016/j.pmatsci.2023.101132>
- [13] Fernandez-Corbaton I et al. New twists of 3D chiral metamaterials. *Adv. Mater.* **31**, 1807742 (2019). <https://doi.org/10.1002/adma.201807742>
- [14] Li X, Yang Z and Lu Z. Design 3D metamaterials with compression-induced-twisting characteristics using shear-compression coupling effects. *Extreme Mech. Lett.* **29** (2019). <https://doi.org/10.1016/j.eml.2019.100471>

- [15] Duan S, Xi L, Wen W and Fang D. A novel design method for 3D positive and negative Poisson's ratio material based on tension-twist coupling effects. *Compos. Struct.* **236** (2020). <https://doi.org/10.1016/j.compstruct.2020.111899>
- [16] Li J, Ha C S and Lakes R S. Observation of squeeze-twist coupling in a chiral 3D isotropic lattice. *Phys. Status Solidi B-Basic Solid State Phys.* (2019). <https://doi.org/10.1002/pssb.201900140>
- [17] Chen Y, Frenzel T, Zhang Q, Kadic M and Wegener M. Cubic metamaterial crystal supporting broadband isotropic chiral phonons. *Phys. Rev. Mater.* **5**, 025201 (2021). <https://doi.org/10.1103/PhysRevMaterials.5.025201>
- [18] Zhao W, Zhu J, Liu L, Leng J and Liu Y. A bio-inspired 3D metamaterials with chirality and anti-chirality topology fabricated by 4D printing. *Int. J. Smart Nano Mater.* **14**, 1-20 (2023). <https://doi.org/10.1080/19475411.2022.2120110>
- [19] Pham M S, Liu C, Todd I and Lertthanasarn J. Damage-tolerant architected materials inspired by crystal microstructure. *Nature* **565**, 305-311 (2019). <https://doi.org/10.1038/s41586-018-0850-3>
- [20] Siddique S H, Hazell P J, Wang H, Escobedo J P and Ameri A A. H. Lessons from nature: 3D printed bio-inspired porous structures for impact energy absorption - A review. *Addit. Manuf.* **58**, 103051 (2022). <https://doi.org/https://doi.org/10.1016/j.addma.2022.103051>
- [21] Frenzel T et al. Large characteristic lengths in 3D chiral elastic metamaterials. *Commun. Mater.* **2** (2021). <https://doi.org/10.1038/s43246-020-00107-w>
- [22] Coulais C, Kettenis C and van Hecke M. A characteristic length scale causes anomalous size effects and boundary programmability in mechanical metamaterials. *Nat. Phys.* **14**, 40-44 (2017). <https://doi.org/10.1038/nphys4269>
- [23] Xu W, Wang L, Liu Z and Zhu P. General assembly rules for metamaterials with scalable twist effects. *Int. J. Mech. Sci.*, 108579 (2023). <https://doi.org/https://doi.org/10.1016/j.ijmecsci.2023.108579>
- [24] Frenzel T, Kopfler J, Jung E, Kadic M and Wegener M. Ultrasound experiments on acoustical activity in chiral mechanical metamaterials. *Nat. Commun.* **10**, 3384 (2019). <https://doi.org/10.1038/s41467-019-11366-8>
- [25] Kaarthik P, Sanchez F L, Avtges J and Truby R L. Motorized, untethered soft robots via 3D printed auxetics. *Soft Matter* **18**, 8229-8237 (2022). <https://doi.org/10.1039/d2sm00779g>
- [26] Ye M, Gao L, Wang F and Li H. A novel design method for energy absorption property of chiral mechanical metamaterials. *Materials* **14**, 5386 (2021). <https://doi.org/10.3390/ma14185386>
- [27] Lipton J I et al. Handedness in shearing auxetics creates rigid and compliant structures. *Science* **360**, 632-635 (2018). <https://doi.org/10.1126/science.aar4586>
- [28] Ha C S, Plesha M E and Lakes R S. Chiral three-dimensional lattices with tunable Poisson's ratio. *Smart Mater. Struct.* **25** (2016). <https://doi.org/10.1088/0964-1726/25/5/054005>
- [29] Jenett B et al. Discretely assembled mechanical metamaterials. *Sci. Adv.* **6**, eabc9943 (2020). <https://doi.org/10.1126/sciadv.abc9943>
- [30] Gao Z et al. Additively manufactured high-energy-absorption metamaterials with artificially engineered distribution of bio-inspired hierarchical microstructures. *Compos. Pt. B-Eng.* **247** (2022). <https://doi.org/10.1016/j.compositesb.2022.110345>
- [31] Wang J, Luo X, Wang K, Yao S and Peng Y. On impact behaviors of 3D concave structures with negative Poisson's ratio. *Compos. Struct.* **298** (2022). <https://doi.org/10.1016/j.compstruct.2022.115999>
- [32] Sharma D and Hiremath S S. Bio-inspired repeatable lattice structures for energy absorption: Experimental and finite element study. *Compos. Struct.* **283**, 115102 (2022). <https://doi.org/https://doi.org/10.1016/j.compstruct.2021.115102>
- [33] Goswami D et al. Mechanical metamaterials with programmable compression-twist coupling. *Smart Mater. Struct.* **30**, 015005 (2021). <https://doi.org/10.1088/1361-665x/abc182>
- [34] Fleisch M et al. Chiral-based mechanical metamaterial with tunable normal-strain shear coupling effect. *Eng. Struct.* **284**, 115952 (2023). <https://doi.org/https://doi.org/10.1016/j.engstruct.2023.115952>
- [35] Meng L et al. An emerging class of hyperbolic lattice exhibiting tunable elastic properties and impact absorption through chiral twisting. *Extreme Mech. Lett.* **40** (2020). <https://doi.org/10.1016/j.eml.2020.100869>
- [36] Wang X, Zhu L, Sun L and Li N. Optimization of graded filleted lattice structures subject to yield and buckling constraints. *Mater. Des.* **206** (2021). <https://doi.org/10.1016/j.matdes.2021.109746>
- [37] Qi D et al. Mechanical behaviors of SLM additive manufactured octet-truss and truncated-octahedron lattice structures with uniform and taper beams. *Int. J. Mech. Sci.* **163**, 105091 (2019). <https://doi.org/10.1016/j.ijmecsci.2019.105091>

- [38] Sun T, Yang S and Lian B, *Finite and instantaneous screw theory in robotic mechanism*. (Springer Nature, 2020).
- [39] Cui H et al. Design and printing of proprioceptive three-dimensional architected robotic metamaterials. *Science* **376**, 1287-1293 (2022). <https://doi.org:10.1126/science.abn0090>
- [40] Lielens G. Micro-macro modeling of structured materials. *PhD thesis*, Université catholique de Louvain, 1999.
- [41] Tamer Y, Toros S and Ozturk F. Numerical and experimental comparison of fractural characteristics of 316L stainless steel. *J. Mater. Eng. Perform.* **32**, 1103-1118 (2023). <https://doi.org:10.1007/s11665-022-07152-1>
- [42] Li Y, Ge Y, Lei J and Bai W. Mechanical properties and constitutive model of selective laser melting 316L stainless steel at different scanning speeds. *Adv. Mater. Sci. Eng.* **2022**, 1-13 (2022). <https://doi.org:10.1155/2022/2905843>
- [43] Ashby M F. The properties of foams and lattices. *Philos. Trans. R. Soc. A-Math. Phys. Eng. Sci.* **364**, 15-30 (2006). <https://doi.org:10.1098/rsta.2005.1678>